Facet-Dependent Kinetics and Energetics of Hematite for Solar Water Oxidation Reactions

Wei Li,[†] Ke R. Yang,[‡] Xiahui Yao,[†,§] Yumin He,[†] Qi Dong,[ ] Gary W. Brudvig,[‡] Victor S. Batista,[‡] and Dunwei Wang*,[†]

[†]Department of Chemistry, Merkert Chemistry Center, Boston College, 2609 Beacon Street, Chestnut Hill, Massachusetts 02467, United States

[‡]Department of Chemistry and Yale Energy Sciences Institute, Yale University, New Haven, Connecticut 06520-8107, United States

S Supporting Information

ABSTRACT: The performance of a photoelectrochemical (PEC) system is highly dependent on the charge separation, transport and transfer characteristics at the photoelectrode| electrolyte interface. Of the factors that influence the charge behaviors, the crystalline facets of the semiconductor in contact with the electrolyte play an important role but has been poorly studied previously. Here, we present a study aimed at understanding how the different facets of hematite affect the charge separation and transfer behaviors in a solar water oxidation reaction. Specifically, hematite crystallites with predominantly {012} and {001} facets exposed were synthesized. Density functional theory (DFT) calculations

revealed that hematite {012} surfaces feature higher OH coverage, which was confirmed by X-ray photoelectron spectroscopy (XPS). These surface OH groups act as active sites to mediate water oxidation reactions, which plays a positive role for the PEC system. These surface OH groups also facilitate charge recombination, which compromises the charge separation capabilities of hematite. Indeed, intensity modulated photocurrent spectroscopy (IMPS) confirmed that hematite {012} surfaces exhibit higher rate constants for both charge transfer and recombination. Open circuit potential (OCP) measurements revealed that the hematite {012} surface exhibits a greater degree of Fermi level pinning effect. Our results shed light on how different surface crystal structures may change surface kinetics and energetics. The information is expected to contribute to efforts on optimizing PEC performance for practical solar fuel synthesis.

KEYWORDS: hematite, photoelectrochemistry, water splitting, kinetics, energetics, facet
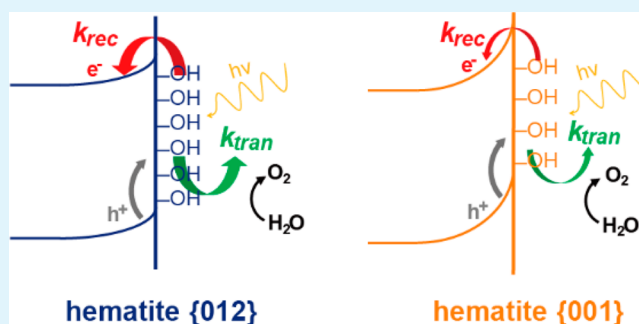
1. INTRODUCTION

Photoelectrochemistry (PEC) represents a process that can directly convert photonic energy to chemical energy and has been widely studied as a potential technology for direct solar fuel synthesis applications.[1,2] For water splitting applications, the key distinguishing feature of a PEC system is the photoelectrode|H_2O interface, where the difference between the Fermi level of the semiconductor and the electrochemical potential of the electrolyte creates a band bending within the semiconductor.[3] The degree of the band bending defines the photo-charge conversion efficiencies. Another critical characteristic of the interface is the efficiency of charge transfer for desired chemical reactions.[4] Together, the electronic properties within the semiconducting photoelectrode and the chemical kinetics at the surface determine the overall performance of a PEC system. It is well-known that the electronic properties of a semiconductor, such as the Fermi level and band edge energetics, are sensitive to the crystal field. The relationship between the facets and the electronic properties of a semiconductor has been extensively studied previously. For

instance, Liu et al. demonstrated that the conduction band edge of anatase TiO_2 crystals with 82% {101} is more negative than that with 72% {001}.[5] Similarly, it is also well accepted that the detailed chemical reactions are dependent on the surface species, which in turn is sensitive to the atomic structures of the substrate. For example, Li et al. found that anatase TiO_2 nanoparticles with predominantly exposed {001} facets have higher photodegradation activity relative to {101} facets, owing to a greater number of 5-fold coordinated Ti^{4+} sites.[6] Taken as a whole, we see that the detailed surface crystal structure of the photoelectrode at the photoelectrode|H_2O interface is of critical importance. To date, how the PEC performance depends on this interface is poorly studied. We aim to address this issue in this Article. Using hematite nanocrystals as a material platform,

we show that {001} facets feature lower surface OH concentrations than {012} facets. The difference in OH concentration is directly correlated to the kinetics at the interface, where the {012} facets exhibit higher rate constants for both charge transfer and recombination. The high surface OH concentrations also imply a higher density of surface states that would pin the Fermi level for the {012} facets to undermine the overall performance, which was directly observed in our experiments.

We chose hematite as a prototypical material platform for this study because a broad knowledge base on this material exists thanks to decades of research by a large number of groups.[7−9] For instance, we have learned that the relatively late turn-on potential of a hematite-based PEC was mainly due to poor charge separation as a result of surface Fermi level pinning.[3] Slow charge transfer kinetics play a relatively smaller role in this regard.[10] We also learned that the surface OH groups play important roles in water oxidation, as well as in cocatalyst deposition.[4,11,12] Notwithstanding, these previous studies have not specifically addressed the dependence of these results on the crystal facets. To address this issue, we built our current study on successes in synthesizing hematite with preferred surfaces by Cha et al. and Chen et al., respectively.[13,14] The materials permitted us to carry out detailed kinetic and thermodynamic studies by intensity modulated photocurrent spectroscopy (IMPS) and open circuit potential (OCP) measurements, which generated quantitative information to support the conclusion that hematite {012} surfaces are more active for charge transfer and recombination than hematite {001} surfaces.

2. EXPERIMENTAL SECTION

2.1. Hematite Synthesis. *Hematite {012}.* Pseudocube hematite nanoparticles with predominately exposed {012} facets were prepared by a hydrothermal method as reported previously.[13] Briefly, $FeCl_3 \cdot 6H_2O$ (Sigma-Aldrich, ACS reagent, 97%) was dissolved into a 0.4 M NaOH (Sigma-Aldrich, ACS reagent, ≥ 97.0%, pellets) solution to make a 0.2 M Fe^{3+} gel solution, with continuous stirring for 10 min at room temperature. The 20 mL gel solution was then transferred into a 25 mL Teflon lined autoclave and heated at 150 °C for 5 h. The as-synthesized hematite nanoparticles were washed with ethanol and deionized (DI) water, and dried at 60 °C in an oven. For convenience of discussions, these samples will be referred as **hematite {012}** henceforth.

Hematite {001}. The synthesis of hexagonal-disc hematite nanoparticles with predominately exposed {001} facets followed the reported method in the literature.[14] Briefly, $FeCl_3 \cdot 6H_2O$ (Sigma-Aldrich, ACS reagent, 97%) was dissolved into a solution of 10 mL of ethanol and 0.7 mL of DI water to make a 1 mM Fe^{3+} gel solution. After the $FeCl_3$ was almost dissolved, 2 g of sodium acetate (Alfa Aesar, anhydrous, ACS, 99.0% min) was added. Then, the gel solution was transferred into a 25 mL Teflon lined autoclave and heated at 180 °C for 12 h. The as-synthesized hematite nanoparticles were washed with ethanol and DI water, and dried at 60 °C in an oven. For convenience of discussions, these samples will be referred to as **hematite {001}** henceforth.

2.2. Characterization of Hematite. Transmission electron micrographs (TEM) showing the exposed facets were taken on a JEOL (model: 2010F) microscope operating at a 200 kV acceleration voltage. Scanning electron micrographs (SEM) showing the morphology were taken on a field-emission JEOL (model: 6340F) operating at a 10 kV acceleration voltage. X-ray photoelectron spectra (XPS) were obtained on a K-Alpha+ instrument (Thermo Scientific) equipped with a microfocused, monochromated Al Kα source (1486.7 eV). All experiments utilized a 50.00 eV pass energy and the acquired spectra were calibrated to the binding energy of C 1s peak at 284.8 eV.

The X-ray diffraction (XRD) measurements were carried out on a Bruker D2 PHASER with a Cu Kα radiation source. Raman spectra were obtained on a Micro-Raman system (XploRA, Horiba) with a 532 nm laser excitation. Light absorption of hematite was collected using a reflectance/transmittance integrating sphere (SphereOptics) and recorded using a spectrometer (Ocean Optics USB 4000).

2.3. Density Functional Theory (DFT) Calculations. DFT calculations were performed with the Vienna ab initio simulation package (VASP).[15] Projector augmented plane wave (PAW) method together with the Perdew-Burke-Ernzerh (PBE) exchange-correlation functional were employed to describe the electron−ion interactions.[16,17] A cutoff of 450 eV was chosen for the plane wave basis set in all calculations. A 5 × 5 × 5 Monckhorst-Pack type k-point grid was chosen for the optimization of bulk Fe_2O_3. The Gaussian smear method was used for Fe_2O_3 with an σ value of 0.1 eV. The energy convergence criterion was set to be 1×10^{-4} eV per unit cell and the geometry convergence criterion was set to be 1×10^{-3} eV per unit cell for energy difference between two consecutive ionic steps. Because of the strong d-electron correlation effects for Fe, the calculations were carried out with the DFT+U method, using the formalism suggested by Dudarev et al.[18] The parameter was set at U_{eff} = 4 eV to reproduce the experimental band gap of α-Fe_2O_3.[19] Slab models of hydroxyl terminated {012} and {001} facets were constructed from the optimized bulk geometry. A 3 × 3 × 1 Monckhorst-Pack type k-point grid was chosen for all slab calculations. A vacuum layer of about 20 Å was used to avoid the interactions between periodic images. The slab model of the hydroxyl terminated {001} facet was chosen to have 4 unit cells with hydroxyl groups on both sides of the slab and full geometry relaxation was performed for this hydroxyl terminated α-Fe_2O_3 slab. The slab model of the hydroxyl terminated {012} facet was constructed to include 4 Fe layers with hydroxyl groups on the top side of the slab. Bottom two layers of ions were fixed at their bulk positions while the top two layers as well as hydroxyl groups were fully relaxed during geometry optimization.

2.4. Electrode Fabrication. A 2.2 mm thick glass slide coated with fluorine-doped tin oxide conductive film (Sigma-Aldrich, 7 Ω/sq surface resistivity) was cleaned in acetone, methanol, isopropanol and DI water. The dried hematite powders were mixed with a 0.3 wt % polyethylenimine (PEI) aqueous ethanol solution (1:1 v/v) to make a 0.5 wt % hematite solution. Hematite nanoparticles were dispersed in an ultrasonic bath for 30 min. Then 30 μL of the hematite solution was dropcasted on a 1×1 cm^2 FTO glass substrate and dried naturally in ambient air at room temperature. The application of PEI was reported to orient the preferably exposed facet of the hematite nanoparticle parallel to the substrate, due to the tension of the polymer during the drying process.[13,20] The FTO glass substrate with monodispersed hematite was then annealed in air at 500 °C to fully convert β-FeOOH to α-Fe_2O_3, removing organic solvents in the hematite solution and improving the adhesion between the hematite nanoparticles and the substrate. To make an photoelectrode, the resulting hematite sample was connected to a Cu wire using Ag paste (MG Chemicals, 8331 Silver Conductive Epoxy Adhesive) and protected with nonconductive epoxy (Loctite 615 Hysol Epoxy Adhesive) to expose an active electrode surface area of ca. 0.16 cm^2.

2.5. PEC Characterization. PEC characterization was carried out using a Solartron ModuLab XM potentiostat. A three-electrode configuration was employed, with hematite as the working electrode, a saturated calomel electrode (SCE, CH instruments, model number: CHI150) as the reference electrode and a Pt wire as the counter electrode. The electrolyte was a 1 M NaOH (Sigma-Aldrich, ACS reagent, ≥ 97.0%, pellets) solution. The light source for all data presented in this work was an AM 1.5 solar simulator (100 mW/cm^2, Solarlight, Model 16S-300-M). In a typical J−V plot, the voltage was swept linearly from negative to positive at a rate of 20 mV s^{-1} with front illumination.

2.6. Intensity Modulated Photocurrent Spectroscopy (IMPS). IMPS spectra were recorded using a Solartron ModuLab XM potentiostat coupled with a Frequency Response Analyzer (FRA, Solartron ModuLab) and a 405 nm LED (ThorLab) with 1000 mA max power and controlled by the ModuLab XM DSSC software. IMPS

data were measured using a 10% light intensity modulation (centered at ca. 134 mW/cm^2) varying between 10 kHz and 0.01 Hz. The same three-electrode configuration and electrolyte were employed as given in the PEC Characterization section.

3. RESULTS AND DISCUSSION

3.1. Structural Differences between Hematite {012} and Hematite {001}. We first show experimental evidence that we have successfully synthesized **hematite {012}** and **hematite {001}**. For this purpose, we used SEM and high-resolution TEM (HRTEM) to study as-synthesized samples, and the representative data are shown in Figure 1. We see in
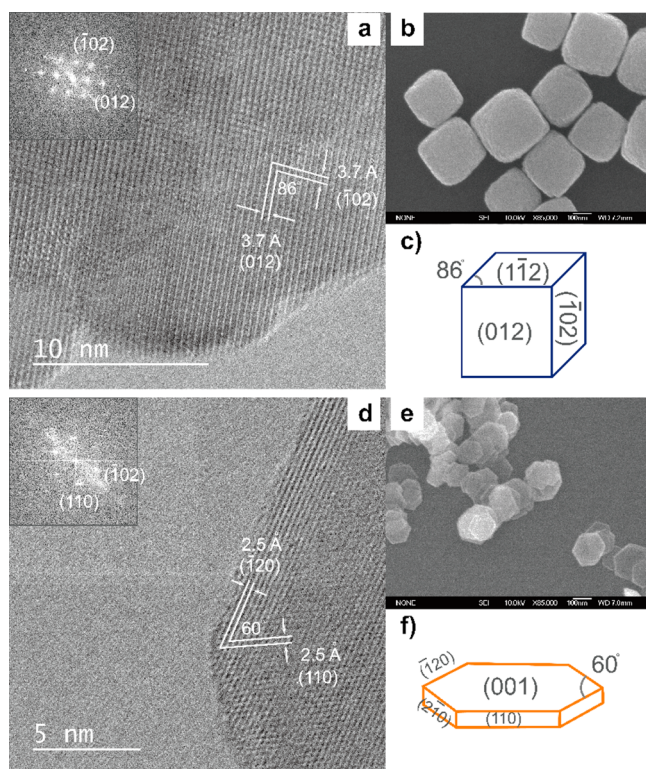

Figure 1. Structural characterization of **hematite {012}** and **hematite {001}**. (a) HRTEM image and (b) SEM image of **hematite {012}**; inset in a: corresponding FFT pattern of the viewing field. (c) Schematic showing the relationships of the front, side and top surfaces of the pseudocube. (d) HRTEM image and (e) SEM image of **hematite {001}**; inset in d: corresponding FFT pattern of the viewing field. (f) Schematic showing the relationship of the side surfaces and the top surface of the hexagonal-plate.

Figure 1b that **hematite {012}** is pseudocubic with a typical size of 200−250 nm. The HRTEM micrograph (Figure 1a) clearly shows two sets of lattice fringes on **hematite {012}**, both evenly spaced at a distance of 3.7 Å. An intersection angle of 86° was measured between the two sets of lattice fringes. The observation is in excellent agreement with expectations for the hematite (012) and ($\bar{1}$02) planes (see the corresponding FFT pattern in Figure 1a inset). The zone axis of Figure 1a was identified as [$2\bar{2}\bar{1}$]. As such, the front, side and top surfaces of the pseudocube are (012), ($\bar{1}$02), and (1$\bar{1}$2) plane, respectively. The relationships between these facets are illustrated schematically in Figure 1c. The hidden planes of the pseudocube as shown in Figure 1c are (0$\bar{1}\bar{2}$), (10$\bar{2}$), and ($\bar{1}1\bar{2}$). Importantly, all six exposed planes are equivalent and belong to the {012} group. We, therefore, concluded that the pseudocubic hematite

preferably exposes the {012} facet. Similarly, as shown in Figure 1e, hematite {001} exhibits a hexagonal disc morphology with a typical size of 150−200 nm and a thickness of 10−15 nm. HRTEM data of **hematite {001}** revealed two sets of lattice fringes, each separated by 2.5 Å. Combining this with the intersection angle of 60°, we assigned these lattice fringes to the {110}, {210}, and {120} planes. Consequently, the basal top and bottom surfaces were unambiguously confirmed to be the {001} planes.

For the study on how the PEC characteristics depend on the facets, it is important to know how the surface chemical species differ for different facets. More specifically, for water oxidation reactions, surface OH species play an important role.[12,21] Previous impedance spectroscopic studies suggested that M−OH$_x$ intermediates is key to building up surface-states capacitance and influences surface charge recombination; on the other hand, OH species has been demonstrated to actively participate in PEC water oxidation on hematite by IR spectroscopic measurements. We, therefore, chose the abundance of surface OH species as a descriptor to quasi-quantitatively compare **hematite {012}** and **hematite {001}**. Density functional theory (DFT) was employed to optimize the geometry of bulk hematite and constructed slab models for these two hematite samples. The hydroxyl terminated {012} and {001} facets were then fully relaxed with DFT and their structures are shown in Figure 2, as well as the lattice vector
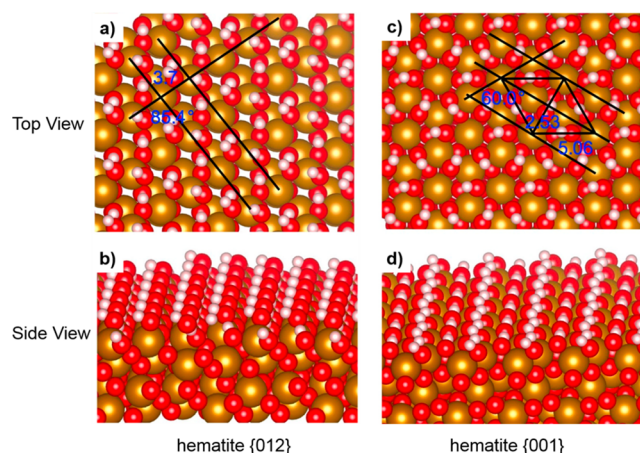
Figure 2. DFT optimized structures of: (a) top view, (b) side view of **hematite {012}** and (c) top view, (d) side view of **hematite {001}**. The lattice vector lengths and angles are given in Angstrom (Å) and degree (deg), respectively. Brown, red, and white balls represent Fe, O, and H atoms.

lengths and angles. Our DFT calculations predict the hematite {012} features higher OH density, the OH densities of {012} and {001} facets being 14.5 and 13.5 nm^{-2}, respectively.

The DFT results are consistent with the characterization by XPS. The O 1s spectra of **hematite {012}** and **hematite {001}** are shown in Figure 3. As reported in the literature, the broad O 1s peak may be deconvoluted into 3 distinct peaks that correspond to surface OH species, lattice OH species and lattice O^{2-} species.[22] The peaks at 529.4 eV for **hematite {012}** and 529.8 eV for **hematite {001}** were assigned to lattice O. The peaks at 530.4 eV for **hematite {012}** and 530.5 eV for **hematite {001}** were assigned to hydroxyl groups due to H binding to lattice O. The peaks at 531.0 eV for **hematite {012}** and 531.2 eV for **hematite {001}** were assigned to surface
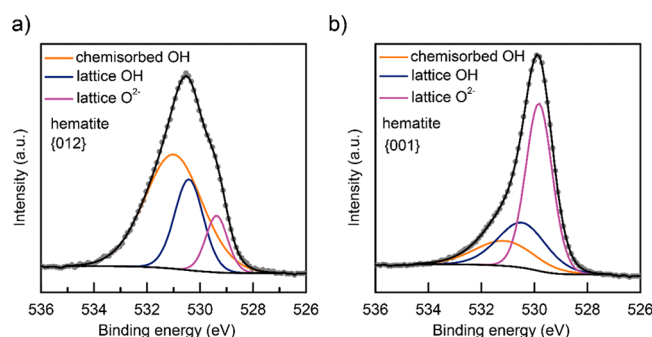
Figure 3. XPS O 1s spectra of: (a) **hematite {012}** and (b) **hematite {001}** showing 3 distinct peaks that correspond to surface OH species, lattice OH species, and lattice O^{2-} species.

adsorbed OH. By comparing the relative areas of the deconvoluted peaks, we were able to quantify the relative abundance of these different species. The results are summarized in Table 1. From this set of data, we clearly see

Table 1. Summary of XPS Peak Position and Relative Abundance of Surface OH Species, Lattice OH Species and Lattice O^{2-} Species

	lattice O^{2-} (abundance %)	lattice OH (abundance %)	chemisorbed OH (abundance %)
{012}	529.4 eV (12%)	530.4 eV (25%)	531.0 eV (63%)
{001}	529.8 eV (55%)	530.5 eV (27%)	531.2 eV (18%)

a stark difference in the abundance of chemisorbed surface OH species (ca. 63% for **hematite {012}**; 18% for **hematite {001}**). The crystallinity and preferable facet exposure were further confirmed by XRD patterns (Figure S1 inS). It is important to note that these two samples feature similar optical absorption properties (Figure S2), making them an ideal platform to study how the different facets influence the PEC performance to be discussed next.

3.2. Comparison of Photoelectrochemical Performance. Next, we measured the PEC performance of monodispersed **hematite {012}** or **hematite {001}** for water oxidation. The method of electrode fabrication was detailed in the Experimental Section. It is noted here that for this body of research, we employed a relatively sparse distribution of hematite nanoparticles (Figure S3; estimated density: 5−7 particles per μm^2). Further increase in the density would lead to bundling of **hematite {001}** discs, hiding the {001} basal planes, which would be dentrimental to our study. The density of **hematite {012}** was kept at a similarly low level for easy direct comparisons. Although there is a direct contact between FTO and the electrolyte, there was no measurable current within the potential window used for this study when bare FTO substrate was used (Figure 4). As such, the shunt current between FTO and the electrolyte contributes little to the measured photocurrents. Moreover, we note that it is beneficial to keep the density of hematite nanoparticles low for this study because higher density would lead to stacking of nanoparticles, in which case the charge transport between different layers of nanoparticles would become another limiting factor, greatly complicating data interpretation.[13,23,24] We thus establish that the photoelectrodes with relatively sparse hematite particles are indeed valid study platforms for the present work.

Figure 4 shows the photocurrent density-potential (J−V) plot of **hematite {012}** and **hematite {001}** under under AM
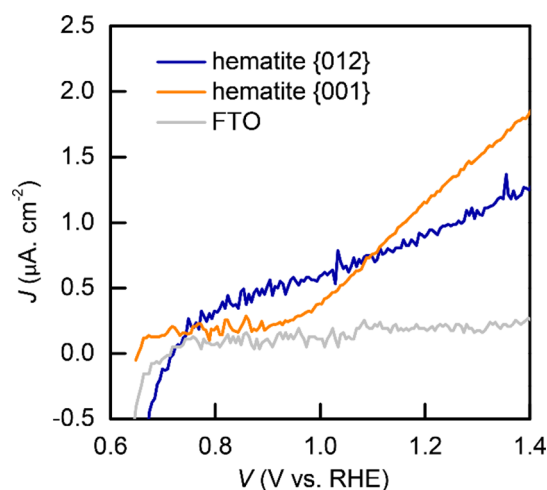

Figure 4. Photocurrent density-potential (J−V) plots of **hematite {012}** and **hematite {001}** under AM 1.5G (100 mW cm^{-2}) illumination in 1 M NaOH (pH 13.6).

1.5G (100 mW•cm^{-2}) illumination in 1 M NaOH (pH 13.6). Both samples exhibited anodic photocurrents due to photo-oxidation of water. Two obvious differences were observed in this set of data. First, **hematite {012}** exhibited an earlier turn-on voltage (0.74 V vs 0.88 V for **hematite {001}**). Second, **hematite {001}** featured a higher photocurrent density at more positive potentials (e.g., at 1.4 V vs RHE, or reversible hydrogen electrode). We are mindful that due to the relative sparseness of the hematite nanoparticles, the photocurrent density should be treated quasi-quantitatively. To support that the trend was indeed statistically significant, we show in Figure S4 that the same trend was observed on 6 different samples. Given that both hematite samples featured similar crystallinity with similar light absorption, we concluded that the difference should originate from the difference in their exposed facets. Guided by this hypothesis, we next present experimental efforts aimed at measuring how the charge transfer (kinetics) and surface band bending (thermodynamics) depend on the different facets of hematite.[10]

3.3. Comparison of Charge Transfer Kinetics. For the comparison, our first task was to measure the kinetics of various charge processes at the surface of hematite. Following earlier studies by us,[4,25,26] we show in Figure 5a a kinetic model used for this work, where the competing charge transfer and recombination kinetics under PEC water oxidation conditions are illustrated. An important assumption for the current study was that water oxidation by hematite is mediated by surface chemisorbed OH species.[12] These species introduce electronic states on the surface. We also assume that hole transfer from the valence band to these surface states is fast and is not rate limiting. Hence, only hole transfer from the surface states to the electrolyte and electron/hole recombination via surface states are considered in our kinetic model. Such a simplification has proven effective in understanding the important characteristics of hematitelelectrolyte interfaces previously.[4,25−27] Higher order processes such as charge transfer to and from the surfaces, as well as the detailed chemical processes, would need to be taken into account for a more detailed kinetic understanding of the system, which is beyond the scope of the current work.

Following our previous reports, we focused our present study on 3 key kinetic parameters, forward charge transfer (k_{tran}),
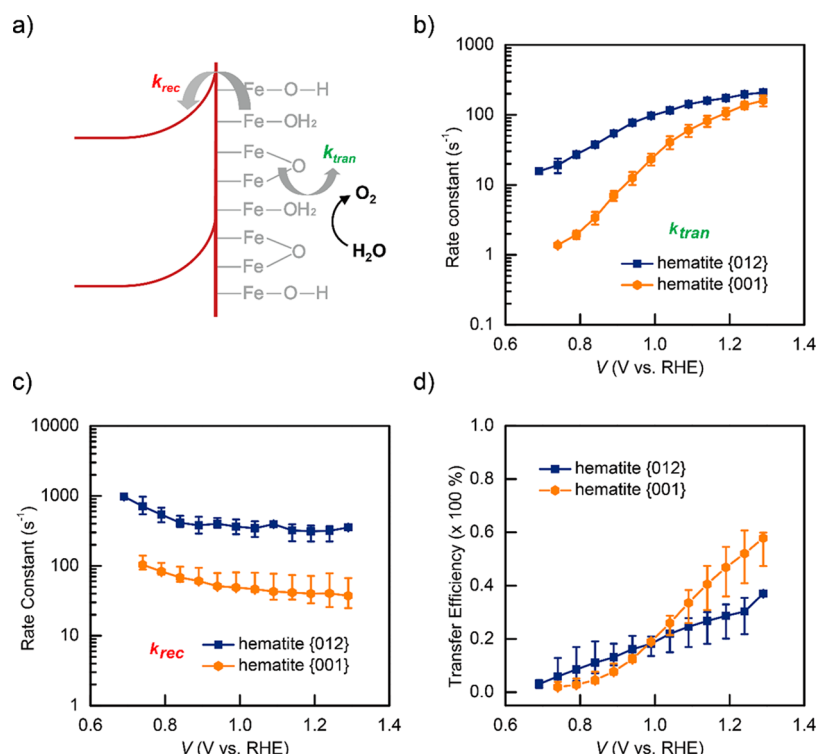
Figure 5. Kinetic comparisons of **hematite {012}** and **hematite {001}**. (a) Kinetic model describing the competing charge transfer and recombination processes under PEC water oxidation conditions. It is assumed that water oxidation by hematite is mediated by surface chemisorbed OH species. Comparisons of: (b) rate constant for charge transfer, (c) rate constant for charge recombination, and (d) charge transfer efficiency for **hematite {012}** and **hematite {001}**, respectively.

backward charge recombination (k_{rec}) and the overall charge transfer efficiency $TE = \left(\frac{k_{tran}}{k_{tran} + k_{rec}}\right)$. Representative data sets of normalized IMPS response as a function of frequency are shown in Figure S5, in which the normalized interception in the low frequency region reports on the charge transfer efficiency; the radial frequency at the maximum of the semicircle corresponds with the sum of ($k_{tran} + k_{rec}$). The data as measured by IMPS are presented in Figure 5. Given the relatively sparse hematite density and the relatively low current densities, we chose to interpret the data quasi-quantitatively. That is, we emphasize the trend but do not wish to discuss the significance of the quantitative differences. Following this guiding principle, we clearly see the following trend in this set of data. First, **hematite {012}** featured higher rate constants for both charge transfer (Figure 5b) and charge recombination (Figure 5c) across the entire potential window. The observation is consistent with our hypothesis that a higher surface OH density would favor water oxidation reactions and, hence, faster charge transfer. The faster charge recombination can be easily understood by a higher density of surface states that would promote charge recombination. Second, within this trend, however, we clearly see the difference of k_{tran}'s between **hematite {012}** and **hematite {001}** becomes much smaller at more positive potentials. This is consistent with the understanding that water oxidation at high applied bias is dominated by the bias, but less sensitive to the chemical nature of the surface. Third, we see that the relative difference of k_{rec} values between **hematite {001}** and **hematite {012}** remain unchanged, whereas both are smaller at higher applied bias. The observation is consistent with previous reports that higher applied bias would suppress recombination. It also supports the

conclusion that the recombination is indeed mediated by surface states, and faster recombination would be expected on surfaces with a higher density of surface states (e.g., **hematite {012}**). Lastly, we note that the trends of TE as shown in Figure 5d are consistent with the JV data as shown in Figure 4, further supporting the suitableness of using IMPS to study this system.

Our understanding of the kinetic differences between **hematite {012}** and **hematite {001}** is summarized in Figure 6. A higher k_{tran} was observed for **hematite {012}** because it
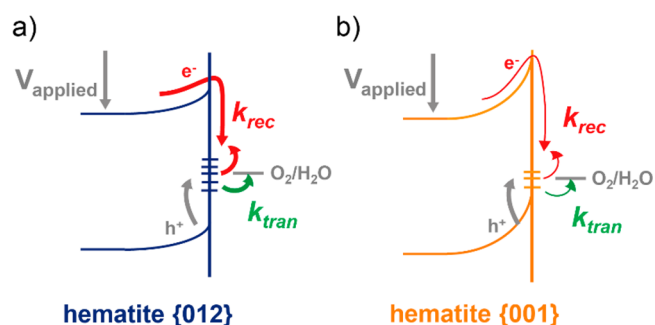
Figure 6. Schematics illustrating the kinetic differences between: (a) **hematite {012}** and (b) **hematite {001}**.

features a higher density of reactive sites. These active sites also serve as charge recombination centers, resulting in higher k_{rec}. This model explains why we observed an earlier turn-on voltage in Figure 4. It also implies that for future improvement of photoelectrode performance, it is critical to increase the active sites to benefit forward charge transfer without simultaneously increasing charge recombination. How to do so remains a
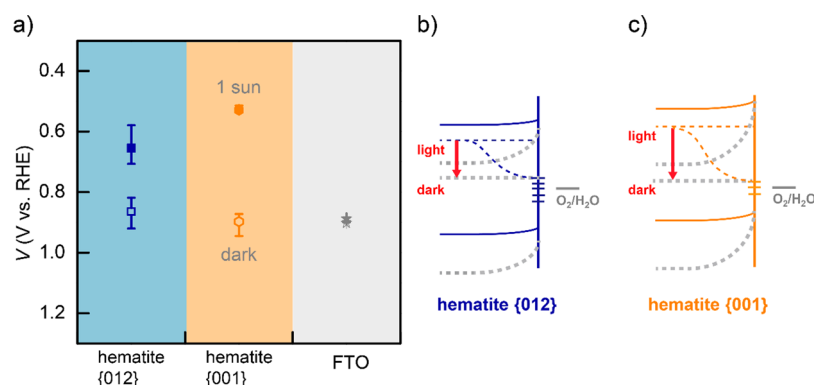
Figure 7. OCP measurements of **hematite {012}** and **hematite {001}**. (a) Comparisons of OCP in dark and in light for **hematite {012}**, **hematite {001}** and FTO. Schematic illustrating the energetic differences between: (b) **hematite {012}** and (c) **hematite {001}**.

critical challenge that deserves additional research. Our recent research of using NiFeO$_x$ catalysts on hematite shed some light on possible solutions to this challenge.[10,25] In addition to the influence of different facets on surface holes transfer, it is also expected to influence electron transport within hematite. As reported by Kerisit et al., electron transport within layers of (001) hydroxyl-terminated surface is faster than (012) surface, but is slower between adjacent layers. The complex model is beyond the scope of this work but worth further research and discussions.

3.4. Comparison of Surface Energetics. With the kinetics of the surface established, we next measured the surface energetics of **hematite {012}** and **hematite {001}** by the OCP technique. Our expectations are as follows. A higher density of surface OH species would lead to a higher density of surface states, which in turn results in a greater extent of Fermi level pinning. We therefore would expect less band bending in **hematite {012}** than **hematite {001}** under illumination. To test this hypothesis, we measured the OCP under dark and light for three different samples, **hematite {012}**, **hematite {001}** and bare FTO as a control. The data are shown in Figure 7a. We emphasize the difference between OCP in dark and in light (ΔOCP), which was 0.21 V for **hematite {012}**, 0.37 V for **hematite {001}** and 0 V for FTO, consistent with our expectations. Within this data set, we note that the dark OCPs for all three samples were comparable, at ca. 0.9 V vs RHE, similar to what we have observed previously on hematite thin films.[3,28] The most striking difference in the OCP was observed under illumination, 0.65 V for **hematite {012}** and 0.53 V for **hematite {001}**. The difference may be attributed to the different natures of the exposed facets. A similar shift was observed on the pseudo flat-band potentials as measured by the Mott−Schottky technique (Figure S6 in SI). Our understanding of this set of data is summarized schematically in Figure 7b, c. In essence, **hematite {001}** features a lower number of surface OH species than **hematite {012}**. Although it is a less active surface for water oxidation, it is also less active for charge recombination. In addition, a larger degree of band bending promises better charge separation. Combining these two facts, **hematite {001}** enables a higher photocurrent at high applied bias.

4. CONCLUSION

In summary, we successfully synthesized hematite nanoparticles with predominately exposed {012} or {001} facets. DFT calculations predicted that the surface crystal structure of these two hematite samples feature different OH concentrations, which is critical to water oxidation under PEC conditions. Indeed, surface characterization using XPS confirmed that **hematite {012}** features higher surface OH concentrations than **hematite {001}**. IMPS analysis revealed that {012} facets exhibit higher rate constants for both charge transfer and recombination. OCP measurements uncovered a more obvious Fermi level pinning effect on {012} facets, due to a higher density of surface states induced by OH species. Together, the detailed kinetic and thermodynamic studies explained the different PEC performance of **hematite {012}** and **hematite {001}**, and highlight the importance of surface structure on determining charge transfer at the photoelectrode|H$_2$O interface. The different k_{tran} observed on different facets would enlighten studies on understanding catalytic mechanism on the basis of exposed facet, or tuning catalytic activity by hierarchical crystalline domains. This work also sheds lights on how to further improve the PEC performance for hematite photoelectrodes. High-performance photoelectrodes will likely feature surface chemical species that improve charge transfer kinetics but do not promote recombination (e.g., heterogenized molecular catalysts).[4,11,19]

XRD spectra of **hematite {012}** and **hematite {001}**; light absorption of **hematite {012}** and **hematite {001}**; SEM showing a relatively sparse distribution of hematite nanoparticles; *JV* plots of **hematite {012}** and **hematite {001}** showing the same trend was observed on 6 samples; representative raw IMPS data of **hematite {012}** and **hematite {001}**; Mott−Schottky plots of **hematite {012}** and **hematite {001}**. The Supporting Information is available free of charge via the Internet at http://pubs.acs.org.

ASSOCIATED CONTENT

Ⓢ Supporting Information

The Supporting Information is available free of charge on the ACS Publications website at DOI: 10.1021/acsami.8b05190.

Figures S1−S6 (PDF)

AUTHOR INFORMATION

Corresponding Author

*E-mail: dunwei.wang@bc.edu.

ORCID Ⓘ

Xiahui Yao: 0000-0001-6258-2382
Qi Dong: 0000-0002-7553-4213
Gary W. Brudvig: 0000-0002-7040-1892

Victor S. Batista: 0000-0002-3262-1237
Dunwei Wang: 0000-0001-5581-8799

Present Address

§X.Y. is currently at Department of Nuclear Science and Engineering, 77 Mass Ave, Cambridge, MA 02139, United States

Author Contributions

W.L and D.W. conceived the project. W.L. carried out most experiments. K.Y. and V.B. carried out DFT calculations. X.Y. and Y.H. carried out TEM experiments. Q.D. carried out XPS measurements. D.W. and G.B. directed the research. W.L. and D.W. wrote the manuscript. All authors have read and commented on the manuscript.

Notes

The authors declare no competing financial interest.

■ ABBREVIATIONS

IMPS, intensity modulated photocurrent spectroscopy; OCP, open circuit potential; PEC, photoelectrochemistry

■ REFERENCES

(1) Walter, M. G.; Warren, E. L.; McKone, J. R.; Boettcher, S. W.; Mi, Q.; Santori, E. A.; Lewis, N. S. Solar Water Splitting Cells. *Chem. Rev.* **2010**, *110*, 6446−6473.

(2) Zhu, S.; Wang, D. Photocatalysis: Basic Principles, Diverse Forms of Implementations and Emerging Scientific Opportunities. *Adv. Energy Mater.* **2017**, *7*, 1700841−1700865.

(3) Du, C.; Yang, X.; Mayer, M. T.; Hoyt, H.; Xie, J.; McMahon, G.; Bischoping, G.; Wang, D. Hematite-Based Water Splitting with Low Turn-on Voltages. *Angew. Chem., Int. Ed.* **2013**, *52*, 12692−12695.

(4) Li, W.; He, D.; Sheehan, S. W.; He, Y.; Thorne, J. E.; Yao, X.; Brudvig, G. W.; Wang, D. Comparison of Heterogenized Molecular and Heterogeneous Oxide Catalysts for Photoelectrochemical Water Oxidation. *Energy Environ. Sci.* **2016**, *9*, 1794−1802.

(5) Liu, G.; Sun, C.; Yang, H. G.; Smith, S. C.; Wang, L.; Lu, G. Q.; Cheng, H.-M. Nanosized Anatase TiO₂ Single Crystals for Enhanced Photocatalytic Activity. *Chem. Commun.* **2010**, *46*, 755−757.

(6) Li, C.; Koenigsmann, C.; Ding, W.; Rudshteyn, B.; Yang, K. R.; Regan, K. P.; Konezny, S. J.; Batista, V. S.; Brudvig, G. W.; Schmuttenmaer, C. A.; Kim, J.-H. Facet-Dependent Photoelectrochemical Performance of TiO₂ Nanostructures: An Experimental and Computational Study. *J. Am. Chem. Soc.* **2015**, *137*, 1520−1529.

(7) Tilley, S. D.; Cornuz, M.; Sivula, K.; Grätzel, M. Light-Induced Water Splitting with Hematite: Improved Nanostructure and Iridium Oxide Catalysis. *Angew. Chem.* **2010**, *122*, 6549−6552.

(8) Ling, Y.; Wang, G.; Wheeler, D. A.; Zhang, J. Z.; Li, Y. Sn-Doped Hematite Nanostructures for Photoelectrochemical Water Splitting. *Nano Lett.* **2011**, *11*, 2119−2125.

(9) Klahr, B.; Gimenez, S.; Fabregat-Santiago, F.; Hamann, T.; Bisquert, J. Water Oxidation at Hematite Photoelectrodes: The Role of Surface States. *J. Am. Chem. Soc.* **2012**, *134*, 4294−4302.

(10) Thorne, J. E.; Li, S.; Du, C.; Qin, G.; Wang, D. Energetics at the Surface of Photoelectrodes and Its Influence on the Photoelectrochemical Properties. *J. Phys. Chem. Lett.* **2015**, *6*, 4083−4088.

(11) Li, W.; Sheehan, S. W.; He, D.; He, Y.; Yao, X.; Grimm, R. L.; Brudvig, G. W.; Wang, D. Hematite-Based Solar Water Splitting in Acidic Solutions: Functionalization by Mono- and Multilayers of Iridium Oxygen-Evolution Catalysts. *Angew. Chem., Int. Ed.* **2015**, *54*, 11428−11432.

(12) Zandi, O.; Hamann, T. W. Determination of Photoelectrochemical Water Oxidation Intermediates on Haematite Electrode Surfaces Using Operando Infrared Spectroscopy. *Nat. Chem.* **2016**, *8*, 778−783.

(13) Cha, H. G.; Kang, M. J.; Hwang, I. C.; Kim, H.; Yoon, K. B.; Kang, Y. S. Manual Assembly of Nanocrystals for Enhanced Photoelectrochemical Efficiency of Hematite Film. *Chem. Commun.* **2015**, *51*, 6407−6410.

(14) Chen, L.; Yang, X.; Chen, J.; Liu, J.; Wu, H.; Zhan, H.; Liang, C.; Wu, M. Continuous Shape- and Spectroscopy-Tuning of Hematite Nanocrystals. *Inorg. Chem.* **2010**, *49*, 8411−8420.

(15) Kresse, G.; Furthmüller, J. Efficient Iterative Schemes for *ab initio* Total-Energy Calculations Using a Plane-Wave Basis Set. *Phys. Rev. B: Condens. Matter Mater. Phys.* **1996**, *54*, 11169−11186.

(16) Kresse, G.; Joubert, D. From Ultrasoft Pseudopotentials to the Projector Augmented-Wave Method. *Phys. Rev. B: Condens. Matter Mater. Phys.* **1999**, *59*, 1758−1775.

(17) Perdew, J. P.; Burke, K.; Ernzerhof, M. Generalized Gradient Approximation Made Simple. *Phys. Rev. Lett.* **1996**, *77*, 3865−3868.

(18) Dudarev, S. L.; Botton, G. A.; Savrasov, S. Y.; Humphreys, C. J.; Sutton, A. P. Electron-Energy-Loss Spectra and the Structural Stability of Nickel Oxide: An LSDA+U Study. *Phys. Rev. B: Condens. Matter Mater. Phys.* **1998**, *57*, 1505−1509.

(19) Zhao, Y.; Yang, K. R.; Wang, Z.; Yan, X.; Cao, S.; Ye, Y.; Dong, Q.; Zhang, X.; Thorne, J. E.; Jin, L.; Materna, K. L.; Trimpalis, A.; Bai, H.; Fakra, S. C.; Zhong, X.; Wang, P.; Pan, X.; Guo, J.; Flytzani-Stephanopoulos, M.; Brudvig, G. W.; Batista, V. S.; Wang, D. Stable Iridium Dinuclear Heterogeneous Catalysts Supported on Metal-Oxide Substrate for Solar Water Oxidation. *Proc. Natl. Acad. Sci. U. S. A.* **2018**, *115*, 2902−2908.

(20) Sugimoto, T.; Muramatsu, A.; Sakata, K.; Shindo, D. Characterization of Hematite Particles of Different Shapes. *J. Colloid Interface Sci.* **1993**, *158*, 420−428.

(21) Klahr, B.; Gimenez, S.; Zandi, O.; Fabregat-Santiago, F.; Hamann, T. Competitive Photoelectrochemical Methanol and Water Oxidation with Hematite Electrodes. *ACS Appl. Mater. Interfaces* **2015**, *7*, 7653−7660.

(22) Baltrusaitis, J.; Cwiertny, D. M.; Grassian, V. H. Adsorption of Sulfur Dioxide on Hematite and Goethite Particle Surfaces. *Phys. Chem. Chem. Phys.* **2007**, *9*, 5542−5554.

(23) Sivula, K.; Zboril, R.; Le Formal, F.; Robert, R.; Weidenkaff, A.; Tucek, J.; Frydrych, J.; Grätzel, M. Photoelectrochemical Water Splitting with Mesoporous Hematite Prepared by a Solution-Based Colloidal Approach. *J. Am. Chem. Soc.* **2010**, *132*, 7436−7444.

(24) Gonçalves, R. H.; Lima, B. H. R.; Leite, E. R. Magnetite Colloidal Nanocrystals: A Facile Pathway to Prepare Mesoporous Hematite Thin Films for Photoelectrochemical Water Splitting. *J. Am. Chem. Soc.* **2011**, *133*, 6012−6019.

(25) Thorne, J. E.; Jang, J.-W.; Liu, E. Y.; Wang, D. Understanding the Origin of Photoelectrode Performance Enhancement by Probing Surface Kinetics. *Chem. Sci.* **2016**, *7*, 3347−3354.

(26) Thorne, J. E.; Zhao, Y.; He, D.; Fan, S.; Vanka, S.; Mi, Z.; Wang, D. Understanding the Role of Co-Catalysts on Silicon Photocathodes Using Intensity Modulated Photocurrent Spectroscopy. *Phys. Chem. Chem. Phys.* **2017**, *19*, 29653−29659.

(27) Klahr, B.; Gimenez, S.; Fabregat-Santiago, F.; Bisquert, J.; Hamann, T. W. Electrochemical and Photoelectrochemical Investigation of Water Oxidation with Hematite Electrodes. *Energy Environ. Sci.* **2012**, *5*, 7626−7636.

(28) Du, C.; Zhang, M.; Jang, J.-W.; Liu, Y.; Liu, G.-Y.; Wang, D. Observation and Alteration of Surface States of Hematite Photoelectrodes. *J. Phys. Chem. C* **2014**, *118*, 17054−17059.